Entrapped Single Tungstate Site in Zeolite for Cooperative Catalysis of Olefin Metathesis with Brønsted Acid Site

Pu Zhao[1†], Lin Ye[1†], Zhenyu Sun[1‡], Benedict T. W. Lo[1], Harry Woodcock[1], Chen Huang[2], Chiu Tang[3], Angus I. Kirkland[2,3], Donghai Mei[4] and Shik Chi Edman Tsang[1*]

[1] Wolfson Catalysis Centre, Department of Chemistry, University of Oxford, Oxford, OX1 3QR, UK.

[2] Department of Materials, University of Oxford, Oxford, OX1 3PH, UK.

[3] Diamond Light Source Ltd, Harwell Science and Innovation Campus, Didcot, OX11 0DE, UK.

[4] Physical and Computational Sciences Directorate & Institute for Integrated Catalysis, Pacific Northwest National Laboratory, Richland, WA, PO Box 999, USA.

ABSTRACT: Industrial olefin metathesis catalysts generally suffer from low reaction rates and require harsh reaction conditions for moderate activities. This is due to their inability to prevent metathesis active sites (MAS) from aggregation and their intrinsic poor adsorption and activation of olefin molecules. Here, isolated tungstate species as single molecular MAS is immobilized inside zeolite pores by Brønsted acid sites (BAS) on the inner surface. It is demonstrated that unoccupied BAS in atomic proximity to MAS enhance olefin adsorption and facilitate the formation of metallocycle intermediates in a stereospecific manner. Thus, effective cooperative catalysis takes place over the BAS-MAS pair inside the zeolite cavity. In consequence, for the cross-metathesis of ethene and *trans*-2-butene to propene, under mild reaction conditions, the propene production rate over WO_x/USY is *ca.* 7,300 times that over the industrial WO_3/SiO_2 based catalyst. A propene yield up to 79% (80% selectivity) without observable deactivation was obtained over WO_x/USY for a wide range of reaction conditions.

1. INTRODUCTION

Olefins are essential feedstocks for the production of many petrochemicals, oleochemicals, polymers and specialty chemicals. Catalytic olefin metathesis is an important reaction in the chemical industry. For example, the cross-metathesis of ethene and 2-butene to propene and the reverse reaction play a significant role in buffering the global supply of ethene and propene. Over the past fifty years, a number of metal oxides including Re_2O_7, MoO_3 and WO_3 supported on SiO_2 and/or Al_2O_3 have been found to be effective as olefin metathesis catalysts under continuous flow conditions.[1] For various reasons, an inexpensive and robust WO_3/SiO_2 based material is the only widely-employed catalyst in the industry for the cross-metathesis of ethene and 2-butene to propene and the reverse reaction. High temperature (300–550°C) and high pressure (> 20 bar) are required for moderate activities to meet the industrial requirement.[1,2] Active site isolation shifting from WO_3 nanocrystals to surface polymeric WO_x and ultimately to isolated WO_x was found to be promising in improving catalytic activity.[3] Considerable efforts have been made on immobilizing isolated organometallic complexes on SiO_2 and/or Al_2O_3 for high activities despite the fact that they tend to aggregate on open surfaces.[4-6] Nonetheless, the industrial application of these catalysts requires further development. Another way to improve the activity of industrial WO_3/SiO_2 based catalyst becomes clear when one studies the fundamental olefin metathesis reaction mechanism. It is generally accepted that olefin metathesis proceeds via metallocycle intermediates in the rate-determining steps (Scheme 1).[1,7,8] The efficient formation of metallocycle intermediates requires fast adsorption of olefin molecules and appropriate alignment between the C=C bond of adsorbed olefin molecules and the W=O/W=C bond of metathesis active sites (MAS) for [2+2] cycloaddition.[7,9,10] This may be difficult to achieve with a catalyst that contains only isolated MAS. There is an indication from previous studies that the introduction of acidic sites to olefin metathesis catalysts can increase the rate of olefin metathesis reaction.[11] Thus, enhanced activity is obtained when supported WO_3 or MoO_3 is blended with zeolites.[12,13] However, the ill-defined interface between bulk acidic zeolite and MAS do not lead to significant rate enhancement, indicating the cooperative catalysis is not yet optimized.

Thus we designed a new type of bifunctional olefin metathesis catalysts by placing an isolated tungstate as WO_x MAS in a zeolite cavity where unoccupied Brønsted acid sites (BAS) are in atomic proximity for efficient cooperative catalysis. As a result, we show for the first time that, at 200°C and 1 bar, the propene production rate over WO_x/USY is ca. 7,300 times that over the industrial WO_3/SiO_2 based catalyst. A propene yield up to 79% with 80% selectivity without observable deactivation can be

achieved over WO_x/USY for a wide range of reaction conditions. The structure of WO_x/USY catalyst was elucidated by synchrotron X-ray powder diffraction (SXRD) and Rietveld refinement, supported by aberration-corrected scanning transmission electron microscopy (STEM), extended X-ray absorption fine structure (EXAFS) spectroscopy, and so on. These characterization results and density functional theory (DFT) calculation suggest that olefin adsorption can be enhanced by unoccupied BAS and the formation of metallocycle intermediates over isolated WO_x MAS can be greatly facilitated by the nearby unoccupied BAS through the appropriate alignment between the C=C bond of adsorbed olefin molecules and the W=O/W=C bond of WO_x MAS for [2+2] cycloaddition. This accounts for the exceptional olefin metathesis rate observed.

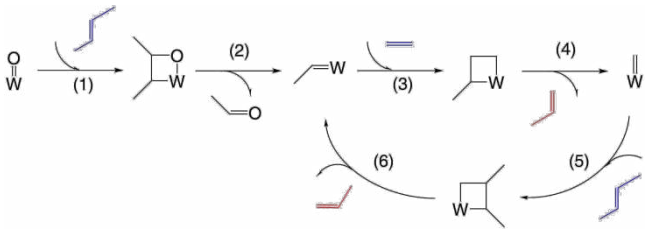

Scheme 1. The reaction mechanism of the cross-metathesis of ethene and *trans*-2-butene to propene over isolated WO_x MAS.[1,7,8] (1, 2) Pseudo-Wittig initiation mechanism for $W{=}CHCH_3$ formation and (3–6) the following metallacyclobutane catalytic cycle to form propene (Chauvin reaction mechanism).

2. EXPERIMENTS

Catalyst preparation. WO_3/SiO_2 was commercially available. WO_x/zeolite catalysts (WO_x/USY, WO_x/ZSM-5, WO_x/SAPO-11, WO_x/SAPO-34 and WO_x/β) were prepared by wet impregnation. USY was obtained from Tosoh. ZSM-5 and β were provided by Sinopec. SAPO-11 and SAPO-34 were purchased from ACS Material. The chemical composition of zeolite supports was analyzed by inductively coupled plasma atomic emission spectroscopy (ICP-AES) or obtained from the literature (Table S1). All zeolites have crystal sizes less than 1 μm. Other chemicals were purchased from Sigma-Aldrich. Typically, 583 mg ammonia metatungstate hydrate ($(NH_4)_6H_2W_{12}O_{40}{\cdot}xH_2O$) was dissolved in 20 mL deionized water before 5 g zeolite was added to the solution. After 1 h magnetic stirring, the dispersion was dried in an 80°C oven overnight. The resulting powder was ground and calcinated at 550°C for 2 h in air. The heating rate was 1°C·min^{-1}. The W loading of WO_x/zeolite catalysts was confirmed to be the same as that of WO_3/SiO_2 by ICP-AES (Table S2). Na^+-poisoned WO_x/USY (WO_x/Na-USY) was prepared by a similar wet impregnation method. Typically, 177 mg sodium nitrate ($NaNO_3$) was used for 5 g WO_x/USY.

Catalytic activity evaluation. The reaction between ethene ($C_2^=$) and *trans*-2-butene (*trans*-2-$C_4^=$) ($n(C_2^=)/n$(*trans*-2-$C_4^=$) = 2/1) was carried out in a stainless steel continuous flow reactor (3/8 in inner diameter and 15 in length). In a typical experiment, 2.1 g catalyst (15–20 cm length) was loaded into the reactor with quartz wool packed at both ends. The catalyst was pretreated with nitrogen (N_2, 16 ml·min^{-1}) at 550°C for 1 h. After the reactor cooled down to the reaction temperature, the reactants, 4% $C_2^=/N_2$ and 2% *trans*-2-$C_4^=/N_2$, were introduced (105 ml·min^{-1} each, weight hourly space velocity (WHSV) = 0.27 h^{-1}, volume hourly space velocity (VHSV) = 26–35 h^{-1}). The flow rates were controlled by Brooks mass flow controllers. The reaction temperature was controlled by a custom-made furnace. The reaction pressure was controlled by a Swagelok back pressure regulator. The products were analyzed online by a Shimadzu GC-2014 gas chromatograph equipped with an SGE BP-1 column (100% dimethylpolysiloxane, 30 m length, 0.53 mm inner diameter, 5.0 μm film thickness) and a flame ionization detector. The *trans*-2-$C_4^=$ conversion, propene ($C_3^=$) selectivity and carbon balance were calculated as follows:

$$\text{Conversion}(\textit{trans}\text{-2-}C_4^=) = \frac{n(\textit{trans}\text{-2-}C_4^= \text{ in feed}) - n(\textit{trans}\text{-2-}C_4^= \text{ remaining})}{n(\textit{trans}\text{-2-}C_4^= \text{ in feed})}$$

$$\text{Selectivity}(C_3^=) = \frac{n(C_3^=)}{n(\text{all products})}$$

$$\text{Carbon balance} = \frac{n(\text{C}) \text{ in products}}{n(\text{C}) \text{ in feed}}$$

$$\text{Yield}(C_3^=) = \text{Conversion}(\textit{trans}\text{-2-}C_4^=) \times \text{Selectivity}(C_3^=) \times \text{Carbon balance}$$

High-resolution STEM. High-resolution electron microscopy was carried out using an aberration-corrected JEOL ARM200F. The microscope was operated at 200 kV in high-angle annular dark-field (HAADF)-STEM mode with HAADF detector collection semi-angles from 73 to 236 mrad. The convergence semi-angle was 31.48 mrad with probe array sizes of 1024 by 1024 and a dwell time of 0.8 μs per pixel. The probe current was 11 pA.

EXAFS and XANES. The local environment of W atoms in WO_x/USY and WO_x/ZSM-5 was probed by analyzing their k^3-weighted W L_3-edge EXAFS spectra collected at beamline B18, Diamond Light Source, UK. The energy resolution ($\Delta E/E$) was $2{\times}10^{-4}$. Fluorescence mode was used. To ascertain data reproducibility, at least two data sets were collected for each sample. W metal was used as a reference to avoid energy shift of the measured EXAFS spectra. Data analysis was performed using IFEFFIT 1 with Horae packages 2 (Athena and Artemis). The amplitude parameter was set as a fixed input parameter to allow the refinement of the coordination number of W. This parameter was obtained from the analysis of the EXAFS spectrum of W metal. First-shell data analysis was performed under the assumption of single scattering with the errors estimated by an *R*-factor. The oxidation states of W in WO_x/USY samples were evaluated by analyzing their k^3-weighted W L_3-edge X-ray absorption near edge structure (XANES) spectra. These XANES spectra were compared with that of $(NH_4)_6H_2W_{12}O_{40}{\cdot}xH_2O$ in which the oxidation state of W is +6.

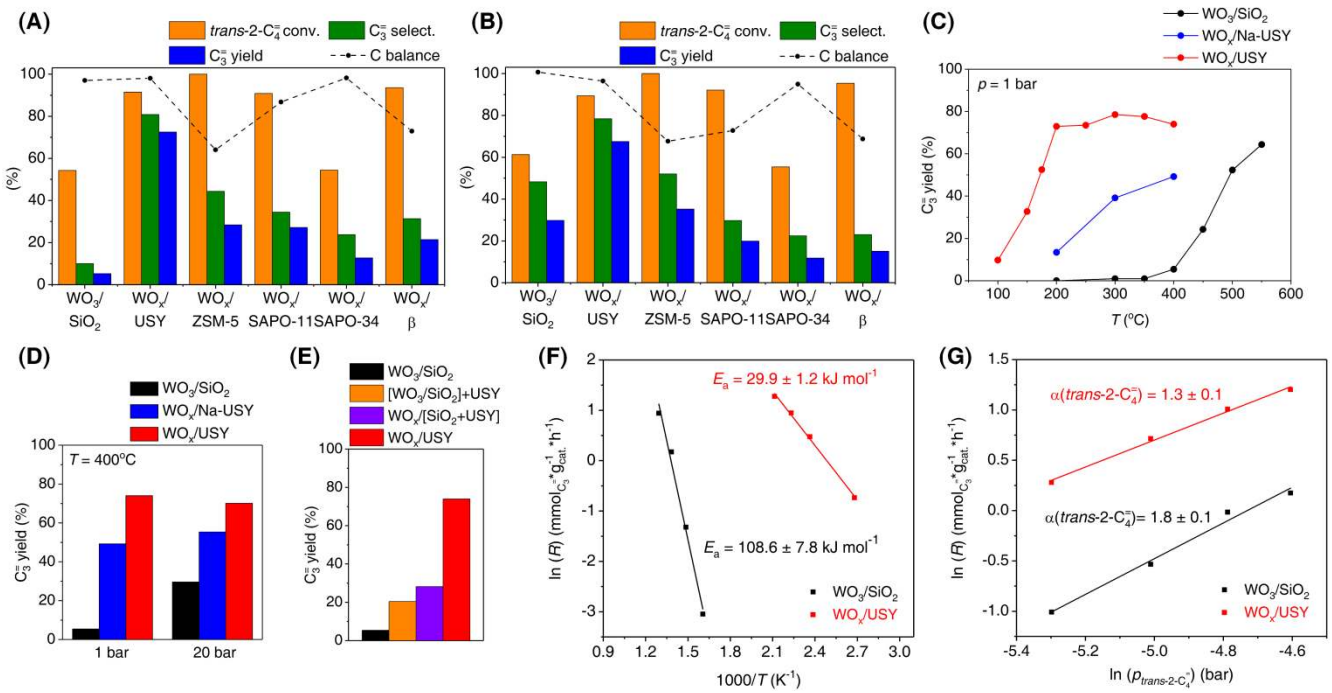

Figure 1. Catalytic activities of WO_x/zeolite catalysts. **(A)** *Trans*-2-butene conversion, propene selectivity, propene yield and carbon balance over WO_x/zeolite catalysts compared to those over WO_3/SiO_2 at T = 400°C, p = 1 and **(B)** 20 bar. Time on steam (TOS) = 1 h. **(C)** Propene yield over WO_3/SiO_2, WO_x/USY and WO_x/Na-USY at T = 100–550°C, p = 1 bar and **(D)** at T = 400°C, p = 1 and 20 bar. TOS = 0.25 h. Carbon balance is above 95% in all experiments. **(E)** Propene yield over WO_3/SiO_2, $[WO_3/SiO_2]$+USY, $WO_x/[SiO_2$+USY] and WO_x/USY at T = 400°C, p = 1 bar. SiO_2 to USY mass ratio = 19/1. TOS = 1 h. Carbon balance is above 95% in all experiments. **(F)** Arrhenius plots for WO_3/SiO_2 and WO_x/USY at T =100–500°C, p = 1 bar. **(G)** Dependencies of propene production rate on the partial pressure of *trans*-2-butene over WO_3/SiO_2 and WO_x/USY at T = 450°C, p = 1 bar. α: order of reaction.

SXRD. High-resolution SXRD data were collected at beamline I11, Diamond Light Source, UK. The energy of the incident X-ray was 15 keV. The wavelength and the 2θ zero point were determined by fitting the diffraction data of high-quality silicon powder (SRM640c). SXRD data were collected for a WO_x/USY sample, a WO_x/ZSM-5 sample, a WO_x/Na-USY sample, and a *trans*-2-butene-adsorbed WO_x/USY (t2be-WO_x/USY) sample. Before data collection, WO_x/USY and WO_x/ZSM-5 was treated under vacuum at 300°C for 2 h. Adsorbed water should have been removed completely. The adsorption of *trans*-2-butene (2% in N_2) on WO_x/USY was performed at room temperature using a Schlenk line. The sample was treated under vacuum at 300°C for 2 h beforehand. Adsorbed water should have been removed completely. Liquid N_2 was used to quench the adsorption of *trans*-2-butene.

All samples were loaded into borosilicate glass capillaries (0.7 mm inner diameter) in a glove box. Glass wool was packed on top of the sample. SXRD data were collected in a Debye-Scherrer geometry using multi-analyzer crystals (MAC) detectors in the 2θ range of 0–150° with 0.001° data binning. Each data set was collected for 1 h for good statistics.

DFT calculation. All periodic calculations were performed using spin-polarized DFT within the generalized gradient approximation (GGA) as implemented in the Vienna ab initio simulation package (VASP).[14-16] The core and valence electrons were represented by the plane-wave basis set using the projector augmented wave (PAW) method[17,18] with a kinetic cutoff energy of 500 eV. The exchange-correlation functional was the Perdew-Burke-Ernzerhof (PBE) functional.[19] Brillouin zone sampling was restricted to Γ point. The energy and force convergence criteria were 1.0×10^{-6} eV and 0.02 eV·Å^{-1} in all structure optimizations. The van der Waals dispersion interaction between the adsorbate and the zeolite framework was included using DFT-D2 scheme.[20] Transition states of elementary steps in the reaction pathways were located using the climbing image nudged elastic band (CI-NEB) method[21,22] and the dimer method[23].

For BAS-catalyzed reaction, the confinement and steric hindrance strongly affect the stabilities of reaction intermediates and transition states.[24] To account for important entropic contribution (ΔS) and zero-point vibrational energy (ΔZPVE) corrections, both Gibbs free energy (ΔG) and enthalpy (ΔH) changes along reaction pathways were calculated as follows:[25,26]

$$\Delta G = \Delta H - T\Delta S$$

$$\Delta H = \Delta U_{trans} + \Delta U_{rot} + \Delta(ZPVE) + \Delta H_{elec}$$

$$\Delta S = \Delta S_{trans} + \Delta S_{rot} + \Delta S_{vib}$$

where translational, rotational, and vibrational contributions to internal energy (ΔU) and entropy (ΔS) were calculated using standard statistical thermodynamic method.[27] The electronic term (ΔH_{elec}) was derived from DFT calculation. The vibrational frequencies of the molecules of interest were calculated in the framework of harmonic oscillator approximation with a displacement of 0.01 Å.

For the calculation of vibrational frequencies, only mobile reaction intermediates over WO_4 MAS as well as first- and second-shell neighboring atoms at BAS were considered. All other atoms of USY framework were fixed. In the estimation of vibrational entropy contribution to Gibbs free energy, the spurious imaginary and low-lying vibrational frequencies (<50 cm^{-1}) that were inevitably obtained in the vibrational frequency calculation were replaced by a normal mode of 50 cm^{-1}.[28-30]

3. RESULTS AND DISCUSSION

Catalytic activities. Laboratory characterization results indicate that WO_x MAS are well dispersed over all WO_x/zeolite catalysts except for WO_x/SAPO-34 (Figs. S1–4, Table S3). Figure 1A shows that the catalytic activities of all WO_x/zeolite catalysts are superior to that of WO_3/SiO_2 at 1 bar, which can be indicative of a synergy between WO_x MAS and the acidic sites in zeolites. Figure 1B shows that the catalytic activity of WO_3/SiO_2 can be significantly improved at 20 bar. This could be due to the increased rate of olefin adsorption over WO_x MAS under higher applied pressure. It is interesting that the catalytic properties of all WO_x/zeolite catalysts remain similar at the two different applied pressures, indicating that olefin adsorption could have readily taken place at a lower pressure in the presence of acidic sites. The difference in the catalyst acidity and zeolite structure can be seen as the primary cause of the variation in the catalytic activities of WO_x/zeolite catalysts. WO_x/ZSM-5, WO_x/SAPO-11 and WO_x/β with high acidic strength and/or large acid quantity (Fig. S5) can give high *trans*-2-butene conversions but low propene selectivities and poor carbon balances. These materials favor the formation of heavy hydrocarbons and carbonaceous deposition due to their strong acidity and characteristic porous structures (Figs. S6–9). Less effective WO_x dispersion is found in WO_x/SAPO-34, as the smaller SAPO-34 pores inhibit the immigration of WO_x during synthesis. This accounts for the lower catalytic activity of WO_x/SAPO-34.

Among all the catalysts studied, WO_x/USY exhibits the highest catalytic activity. As shown in Figs. 1C and 1D, with WO_3/SiO_2 as a reference, WO_x/USY achieves significantly and consistently higher *trans*-2-butene conversions (85–92%), propene selectivities (78–88%) and propene yields (70–79%) over a wide range of reaction conditions (T = 200–400°C, p = 1–20 bar). WO_x/USY also shows good stability for at least 20 hours in our academic laboratory (Fig. S10). Under mild conditions (T = 200°C, p = 1 bar), the propene production rate over WO_x/USY (3.5 $mmol \cdot g_{cat.}^{-1} \cdot h^{-1}$) is *ca.* 7,300 times that over the industrial WO_3/SiO_2 based catalyst (4.8×10^{-4} $mmol \cdot g_{cat.}^{-1} \cdot h^{-1}$) (See SI for rate calculation and number of active sites). We attribute this unprecedented high reaction rate over WO_x/USY to the isolation of WO_x MAS in zeolite pores and the placement of WO_x MAS in atomic proximity to BAS for highly efficient cooperative catalysis of olefin metathesis.

Isolated WO_x MAS. The isolation of WO_x MAS in USY pores was confirmed by high-resolution STEM. Isolated W-containing species can be clearly identified in the HAADF-STEM image of WO_x/USY (Figs. 2A, 2B and S11). They appear to locate inside USY pores. USY framework underwent significant radiation damage during the image acquisition process due to the well-known electron beam sensitivity of zeolites.[31,32] Thus it is acceptable that part of the W-containing species aggregated and formed small clusters on the particle surface with increased electron beam exposure and consequent damage. Isolated WO_x MAS was subsequently revealed to be a discrete molecular dioxo tungstate $(O=)_2W(-O)_2$ (WO_4 MAS) by the best fitting of the k^3-weighted W L_3-edge EXAFS spectra of WO_x/USY (Figs. 2C, S12 and S13, Tables 1 and S4).

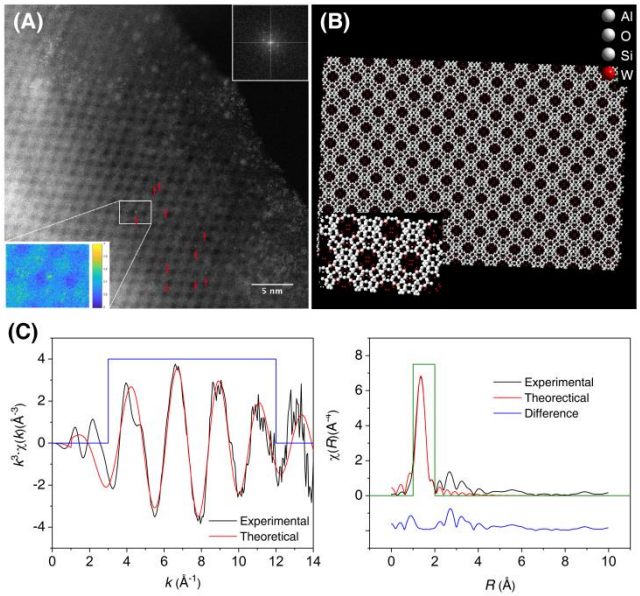

Figure 2. Isolated WO_x MAS. (A) HAADF-STEM image of WO_x/USY. The typical USY pores along zone axes [1 1 0] are shown to be filled with atomic W-containing species (red arrows). The lower left inset shows an enlarged area where the W-containing species is clearly visible. **(B)** Crystallographic model of WO_x/USY from Rietveld refinement (also see Figure 3). The locations of W are in good agreement with those found in the STEM image. **(C)** k^3-weighted W L_3-edge EXAFS spectra of WO_x/USY. k-range for fitting is 3–12 $Å^{-1}$. R-range for fitting is 1–2 Å.

Table 1. Structural data for WO_x MAS in WO_x/USY from its best fitted k^3-weighted W L_3-edge EXAFS spectra.

Scattering path	R = 0.3%, E_{not} = 4.1		
	Bond length (Å)	Coordination number	Debye-Waller factor
W–O1	1.75(1)	2.2(1)	0.003(1)
W–O2	1.90(2)	0.8(1)	0.003(2)
W–O3	2.12(1)	1.1(2)	0.006(2)

It is anticipated that WO_4 MAS inside USY pores may interact with BAS nearby. This is illustrated by comparing the catalytic activities of WO_x/USY and WO_x/Na-USY

(Figs. 1C and 1D). In the absence of BAS (H^+ replaced by Na^+), WO_x/Na-USY clearly delivers inferior catalytic activity to WO_x/USY despite its catalytic activity is still superior to that of WO_3/SiO_2. This supports our hypothesis that BAS in zeolite work in synergy with WO_4 MAS to enhance the overall catalytic activity. As shown in Fig. 1E, the catalytic activity of our bifunctional catalyst is critically dependent on the interface between WO_4 MAS and BAS. The physical mixture of WO_3/SiO_2 and USY ([WO_3/SiO_2]+USY) and the WO_x-deposited mixture of SiO_2 and USY (WO_x/[SiO_2+USY]) have an ill-defined interface between WO_4 MAS and BAS. Thus, they are far less active than WO_x/USY in the cross-metathesis of ethene and *trans*-2-butene to propene. The high catalytic activity of WO_x/USY appears to be due to the effective interaction(s) between WO_4 MAS and BAS inside zeolite.

WO_4 MAS and BAS in atomic proximity. To confirm that WO_4 MAS and BAS are in atomic proximity in USY pores for high catalytic activity, SXRD combined with Rietveld refinement was employed to elucidate the spatial relationships between WO_4 MAS and BAS in WO_x/USY. It is difficult to visualize local 3-dimensional atomic interaction(s) by traditional spectroscopic techniques, *e.g.* UV-Vis, Raman, infrared, electron paramagnetic resonance and X-ray absorption spectroscopy, which are commonly used for olefin metathesis catalyst characterization.[3,11,33,34] This information is also essential when developing an understanding of the cooperative catalysis within a confined zeolite cavity.[35-37]

The structural details of unmodified USY along with the strength, quantity, and location of BAS have been reported in our previous work.[38] BAS (H^+) locates on O4 of USY framework with various strength. We determined the location of WO_4 MAS in USY by refining the crystal structure of WO_x/USY using Rietveld method in TOPAS-Academic 5[39] based on its high-resolution SXRD data. See SI for general Rietveld refinement procedure. The rigid bodies describing WO_4 MAS were built based on EXAFS results and were added into USY framework one by one, following the indication from difference Fourier map. Weighted-profile *R*-factor (R_{wp}) and goodness-of-fit (GOF) were used to gauge the quality of Rietveld refinement. After the first WO_4 rigid body was added, R_{wp} and GOF were found to decrease, indicating the addition of WO_4 rigid body was appropriate. The site occupancy of the second WO_4 rigid body added turned to be almost zero. Thus, the existence of the second WO_4 rigid body was not considered. As a result, one WO_4 rigid body was used to fit the SXRD data (Figs. 3A and S14). The resulting crystallographic model of WO_x/USY (Fig. 2B) matches with its STEM images (Figs. 2A and S11).

It is shown that the isolated WO_4 MAS is trapped in USY cavity by W–O···(H)O4 hydrogen bonding (O_{WO4}···O4 = 2.73(1) Å) on the inner surface (Figs. 3C and 3D). DFT calculation indicates the interaction energy between WO_4 MAS and (H)O4 (BAS) is -141 kJ·mol^{-1} (See DFT calculation section and SI for details). The BAS directly bound to WO_4 MAS has been demonstrated to be reinforced by the extra-framework Al^{3+} (EFAl) in the sodalite cage due to the polarization effect of EFAl on O4.[38] These strong BAS (sBAS) are fully taken up by WO_4 MAS for immobilization according to their resolved site occupancies (sBAS: 2.1 per unit cell (u.c.), WO_4 MAS: 2.8 per u.c.). There are remaining weak BAS (wBAS: 5.1 per u.c.) in close proximity to the immobilized WO_4 MAS in USY cavity. The unoccupied wBAS in WO_x/USY can be selectively replaced by Na^+. This is confirmed by the crystallographic position and resolved site occupancy (5.0 per u.c.) of Na^+ in WO_x/Na-USY (Fig. 3E, see SI for detailed Rietveld refinement procedure and Fig. S15 for data fitting). As described previously, the inhibition of wBAS results in a dramatic decrease in catalytic activity. This reflects the important role of unoccupied BAS in atomic proximity to WO_4 MAS for enhanced reaction rates.

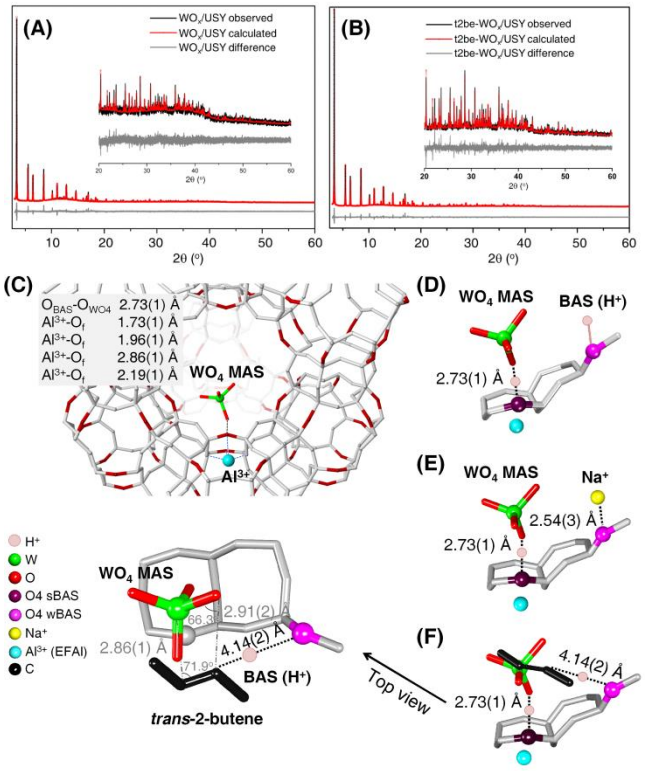

Figure 3. Structure of WO_x/USY. SXRD data of **(A)** WO_x/USY and **(B)** *trans*-2-butene-adsorbed WO_x/USY, fitted by Rietveld refinement. Data in the 2θ range of 20–60° are zoomed in to illustrate the quality of Rietveld refinement. **(C)** Crystallographic model of WO_x/USY from Rietveld refinement. Although H is invisible in SXRD, O4 of USY, where BAS (H^+) locate, are shown in red. **(D)** WO_4 MAS immobilized through hydrogen bonding to (H)O4 of USY. Dummy H^+ is added for illustration. **(E)** The crystallographic position of Na^+ in WO_x/Na-USY (replacing H^+). **(F)** *Trans*-2-butene adsorbed on WO_x/USY showing significant interaction(s) between its double bond, unoccupied BAS, and W=O of WO_4 MAS to form the stereospecific adsorption geometry shown.

We also found a similar entrapment and site isolation of WO_4 MAS in WO_x/ZSM-5 (see SI for detailed explanation, Figs. S16-18 and Table S5) and unoccupied BAS were also shown to be present. We expect that acid quantity, distribution, and strength will significantly affect the ad-

sorption kinetics of olefin molecules, hence influencing the overall olefin metathesis rate over nearby WO_4 MAS. Strong unoccupied BAS in zeolites with stereospecific arrangements may also catalyze side reactions such as isomerization, undesirable cracking, heavy hydrocarbon formation and/or carbon deposition, leading to poor propene selectivity and rapid catalyst deactivation, as in the case of WO_x/ZSM-5. The weak unoccupied BAS in WO_x/USY guarantees high olefin metathesis catalytic activity and stability of the catalyst without significant side products and extensive carbon formation. In addition, the weak unoccupied BAS in WO_x/USY appear to be capable of catalyzing 1-butene (present in industrial reformate gases) to form 2-butene which participates in the cross-metathesis reaction with ethene to form propene. As a result, *ca.* 55% propene yield with *ca.* 95% 1-butene conversion can be achieved over WO_x/USY at 400°C and 1 bar. This reflects the highly cooperative adsorption-metathesis mechanism in this well-designed catalyst.

Cooperative catalysis over the BAS-MAS pair. Effective cooperative catalysis over the BAS-MAS pair is envisaged to be due to the appropriate alignment between the C=C bond of olefin molecules adsorbed over BAS and the W=O bond of WO_4 MAS. To confirm this hypothesis, *trans*-2-butene was loaded in WO_4/USY for the study of its adsorption geometry by SXRD and Rietveld refinement (Fig. 3B, see SI for detailed Rietveld refinement procedure and Fig. S19 for data fitting). The *trans*-2-butene molecule was found to be adsorbed over the unoccupied BAS with an $O4(H)\cdots C^{=}_{t2be}$ distance of 4.14(2) Å (t2be: *trans*-2-butene) (Fig. 3F). This distance is expected for a significant interaction between the electron-rich C=C bond of *trans*-2-butene and the unoccupied BAS (H^+). This could easily lead to the protonation of *trans*-2-butene at elevated temperature.[40]

Perhaps, the most intriguing observation is that the C=C bond of *trans*-2-butene appears to have aligned with the W=O bond of nearby WO_4 MAS at room temperature with a noticeable interaction ($W_{WO4}\cdots C^{=}_{t2be}$ = 2.86(1) Å). The C=C bond of *trans*-2-butene and the W=O bond of WO_4 MAS show a distorted square arrangement, which resembles the anticipated oxametallocycle intermediate formed in the initiation step (Pseudo-Wittig initiation mechanism, Scheme 1). The oxametallocycle intermediate will lead to the formation of a reactive W carbene ($W{=}CHCH_3$) to start the metallacyclobutane catalytic cycle for catalytic olefin metathesis (Chauvin reaction mechanism, Scheme 1). In the metallacyclobutane catalytic cycle, it is envisaged that BAS facilitates the adsorption and alignment of ethene to the nearby W carbene with stereospecificity in a similar manner to form a metallocyclobutane intermediate before propene is produced.

DFT calculation. DFT calculation was carried out to study the metallacyclobutane catalytic cycle. USY model ($T_{192}O_{384}$, T = Si or Al) was built based on our previous work.[38] It has a lattice parameter of 24.2680 Å and 7 BAS. 9 Si^{4+} at specific framework T sites were replaced by Al^{3+} and 2 extra-framework Al^{3+} were added in the sodalite cage. The resulting negatively charged USY framework was compensated by adding 7 H^+ at the O^{2-} directly connected to Al^{3+} (framework) and adding $2[(O{=})_2W(-O)_2]^{2-}$ (WO_4 MAS) at random positions. These added H^+ are active BAS of USY. Structure optimization shows that WO_4 MAS inside USY are most likely bound to H–O4 of the framework (Fig. S20). This is in line with the results from Rietveld refinement.

We first calculated the adsorption and conversion of ethene and *trans*-2-butene over WO_4 MAS, in order to determine which of the two, $W{=}CH_2$ and $W{=}CHCH_3$, is the intermediate to initiate the metallacyclobutane catalytic cycle. As shown in Fig. S21, the formation of the $W{=}CHCH_3$ from *trans*-2-butene is thermodynamically more favored due to its lower Gibbs reaction energies. In particular, the formation of $W{=}CHCH_3$ in the presence of an unoccupied neighboring BAS is kinetically feasible. Therefore $W{=}CHCH_3$ with unoccupied BAS nearby was used as the intermediate to initiate the metallacyclobutane catalytic cycle.

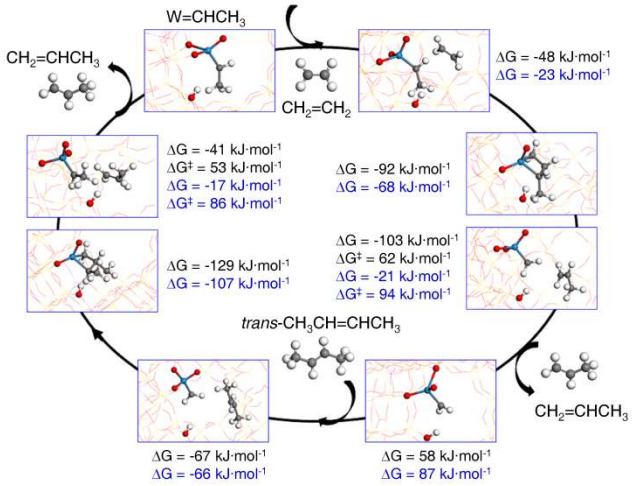

Figure 4. Energy diagram of the metallacyclobutane catalytic cycle over W carbene ($W{=}CHCH_3$) in WO_x/USY. Numbers in black and blue are DFT calculated Gibbs free energies in the presence and absence of an unoccupied BAS near $W{=}CHCH_3$, respectively. The optimized structures in the presence of an unoccupied neighboring BAS are shown.

Figure 4 shows the energy diagram of the metallacyclobutane catalytic cycle over $W{=}CHCH_3$ in the presence/absence of an unoccupied BAS nearby. The metallacyclobutane catalytic cycle is initialized by ethene being adsorbed at $W{=}CHCH_3$ to form a W cyclobutane intermediate. This is followed by the concerted C–C and W–C bond scissions leading to the formation of the first propene. This step is exothermic with a reaction energy (ΔG) of -21 kJ·mol^{-1} in the absence of BAS. The calculated Gibbs energy of activation ($\Delta G^{\ddagger}$) is 94 kJ·mol^{-1}. This is comparable to the experimental apparent activation energy (E_a) obtained for WO_3/SiO_2 which does not have BAS close to its MAS (108.6 kJ·mol^{-1}, Fig. 1F). This kinetically relevant step in the first half of the metallacyclobutane catalytic cycle is significantly promoted when an unoccu-

pied neighboring BAS is present. A dramatically low $\Delta G^{\ddagger}$ (62 kJ·mol^{-1}) was obtained and the concerted C–C and W–C bond scissions are more exothermic (ΔG = -103 kJ·mol^{-1}). The cooperation between the active W=CHCH$_3$ and the unoccupied neighboring BAS is shown to play a key role in increasing olefin metathesis reaction rate, despite that the experimental E_a for WO$_x$/USY (29.9 kJ·mol^{-1}, Fig. 1F) cannot allow a direct comparison with the activation barrier obtained from DFT calculation. The value of experimental E_a is indicative of diffusion limitation which leads to a complex rate-temperature relationship.[41] Upon releasing the first propene, a reactive W=CH$_2$ is formed and is ready for the adsorption of *trans*-2-butene to form a W cyclobutane intermediate subsequently. It is found that the adsorption of *trans*-2-butene and the formation of the W cyclobutane intermediate are affected by the presence of the unoccupied neighboring BAS. More importantly, the calculated $\Delta G^{\ddagger}$ of the second concerted C–C and W–C bond scissions in the presence of the unoccupied neighboring BAS (53 kJ·mol^{-1}) is much lower than that without BAS present (86 kJ·mol^{-1}).

The order of reaction with respect to *trans*-2-butene in excessive ethene was evaluated for WO$_3$/SiO$_2$ (1.8 ± 0.1) and WO$_x$/USY (1.3 ± 0.1), respectively (Fig. 1G). The apparent higher order of reaction with respect to *trans*-2-butene in the case of WO$_3$/SiO$_2$ again suggests WO$_3$/SiO$_2$ has a stronger dependence on the availability of adsorbed olefin. This reflects the higher activation energy process of surface *trans*-2-butene adsorption is rather difficult to proceed in WO$_3$/SiO$_2$. In contrast, as demonstrated, the presence of unoccupied BAS in USY makes a significant contribution to increasing the availability of *trans*-2-butene (with a lower E_a and a lower order of reaction, Fig. 1F and Fig. 1G) and ethene to WO$_4$ MAS in the atomic vicinity. Thus both experimental and theoretical evaluations suggest that the cooperative catalysis between BAS and MAS lead to an overall enhanced catalytic activity.

4. CONCLUSIONS

We have designed a new type of bifunctional olefin metathesis catalysts by immobilizing isolated single WO$_4$ MAS in a zeolite cavity where unoccupied BAS are in atomic proximity. Within the confined zeolite cavity, we demonstrate that BAS facilitate the adsorption and activation of olefin molecules for the metathesis reaction over WO$_4$ MAS. This leads to a dramatically enhanced olefin metathesis reaction rate. We report exceptional propene production rate and thermal stability of WO$_x$/USY under industrially applicable conditions. In general, the concept of cooperative catalysis presented here, using two active sites of different functionalities within atomic proximity in a molecular cavity, can provide new opportunities for designing synergistically adsorptive and catalytic materials.

ASSOCIATED CONTENT

Supporting Information. Methods and additional results of catalyst testing, structure refinement, physical characterization, and suggested future work supplied as Supporting Information. This material is available free of charge via the Internet at http://pubs.acs.org.

AUTHOR INFORMATION

Corresponding Author

* edman.tsang@chem.ox.ac.uk

Author Contributions

† contributed equally as co-first author.

Present Addresses

‡ College of Chemical Engineering, Beijing University of Chemical Technology, China.

ACKNOWLEDGMENT

The STEM, EXAFS and SXRD facilities provided by Diamond Light Source (UK) are acknowledged.

REFERENCES

(1) Lwin, S.; Wachs, I. E., *ACS Catal.* **2014,** *4* (8), 2505-2520.

(2) Mol, J. C., *J. Mol. Catal. A: Chem.* **2004,** *213* (1), 39-45.

(3) Lwin, S.; Li, Y.; Frenkel, A. I.; Wachs, I. E., *ACS Catal.* **2016,** *6* (5), 3061-3071.

(4) Copéret, C.; Comas-Vives, A.; Conley, M. P.; Estes, D. P.; Fedorov, A.; Mougel, V.; Nagae, H.; Núñez-Zarur, F.; Zhizhko, P. A., *Chem. Rev.* **2016,** *116* (2), 323-421.

(5) Mazoyer, E.; Szeto, K. C.; Merle, N.; Norsic, S.; Boyron, O.; Basset, J.-M.; Taoufik, M.; Nicholas, C. P., *J. Catal.* **2013,** *301*, 1-7.

(6) Balcar, H.; Čejka, J., *Coord. Chem. Rev.* **2013,** *257* (21–22), 3107-3124.

(7) Grubbs, R. H.; Wenzel, A. G.; O'Leary, D. J.; Khosravi, E. *Handbook of Metathesis,* Wiley-VCH, Weinheim, 2015.

(8) Hérisson, J.-L.; Chauvin, Y., *Makromol. Chem.* **1971,** *141* (1), 161-176.

(9) Cheng, Z.; Lo, C. S., *ACS Catal.* **2015,** *5* (1), 59-72.

(10) Cheng, Z.; Lo, C. S., *ACS Catal.* **2012,** *2* (3), 341-349.

(11) Amakawa, K.; Wrabetz, S.; Kröhnert, J.; Tzolova-Müller, G.; Schlögl, R.; Trunschke, A., *J. Am. Chem. Soc.* **2012,** *134* (28), 11462-11473.

(12) Huang, S.; Liu, S.; Xin, W.; Bai, J.; Xie, S.; Wang, Q.; Xu, L., *J. Mol. Catal. A: Chem.* **2005,** *226* (1), 61-68.

(13) Li, X.; Zhang, W.; Liu, S.; Xu, L.; Han, X.; Bao, X., *J. Catal.* **2007,** *250* (1), 55-66.

(14) Kresse, G.; Furthmuller, J., *Comput. Mater. Sci.* **1996,** *6* (1), 15-50.

(15) Kresse, G.; Furthmuller, J., *Phys. Rev. B* **1996,** *54* (16), 11169-11186.

(16) Kresse, G.; Hafner, J., *Phys. Rev. B* **1994,** *49* (20), 14251-14269.

(17) Blochl, P. E., *Phys. Rev. B* **1994,** *50* (24), 17953-17979.

(18) Kresse, G.; Joubert, D., *Phys. Rev. B* **1999,** *59* (3), 1758-1775.

(19) Perdew, J. P.; Chevary, J. A.; Vosko, S. H.; Jackson, K. A.; Pederson, M. R.; Singh, D. J.; Fiolhais, C., *Phys. Rev. B* **1992,** *46* (11), 6671-6687.

(20) Grimme, S.; Antony, J.; Ehrlich, S.; Krieg, H., *J. Chem. Phys.* **2010,** *132* (15), 154104.

(21) Henkelman, G.; Uberuaga, B. P.; Jonsson, H., *J. Chem. Phys.* **2000,** *113* (22), 9901-9904.

(22) Mills, G.; Jonsson, H.; Schenter, G. K., *Surf. Sci.* **1995,** *324* (2-3), 305-337.

(23) Henkelman, G.; Jónsson, H., *J. Chem. Phys.* **1999,** *111* (15), 7010-7022. 35.

(24) Gounder, R.; Iglesia, E., *Acc. Chem. Res.* **2012,** *45* (2), 229-238.
(25) Mei, D.; Lercher, J. A., *AIChE J.* **2017,** *63* (1), 172-184.
(26) Zhi, Y.; Shi, H.; Mu, L.; Liu, Y.; Mei, D.; Camaioni, D. M.; Lercher, J. A., *J. Am. Chem. Soc.* **2015,** *137* (50), 15781-15794.
(27) Psofogiannakis, G.; St-Amant, A.; Ternan, M., *J. Phys. Chem. B* **2006,** *110* (48), 24593-24605.
(28) Alexopoulos, K.; Lee, M. S.; Liu, Y.; Zhi, Y. C.; Liu, Y. S.; Reyniers, M. F.; Marin, G. B.; Glezakou, V. A.; Rousseau, R.; Lercher, J. A., *J. Phys. Chem. C* **2016,** *120* (13), 7172-7182.
(29) Piccini, G.; Alessio, M.; Sauer, J.; Zhi, Y.; Liu, Y.; Kolvenbach, R.; Jentys, A.; Lercher, J. A., *J. Phys. Chem. C* **2015,** *119* (11), 6128-6137.
(30) Piccini, G.; Sauer, J., *J. Chem. Theory Comput.* **2014,** *10* (6), 2479-2487.
(31) Pan, M.; Crozier, P. A., *Ultramicroscopy* **1993,** *48* (3), 332-340.
(32) Terasaki, O.; Ohsuna, T.; Ohnishi, N.; Hiraga, K., *Curr. Opin. Solid State Mater. Sci.* **1997,** *2* (1), 94-100.
(33) Ross-Medgaarden, E. I.; Wachs, I. E., *J. Phys. Chem. C* **2007,** *111* (41), 15089-15099.
(34) Basrur, A. G.; Patwardhan, S. R.; Was, S. N., *J. Catal.* **1991,** *127* (1), 86-95.
(35) Ye, L.; Song, Q.; Lo, B. T. W.; Zheng, J.; Kong, D.; Murray, C. A.; Tang, C. C.; Tsang, S. C. E., *Angew. Chem. Int. Ed.* **2017,** *56* (36), 10711-10716.
(36) Teixeira, I. F.; Lo, B. T. W.; Kostetskyy, P.; Stamatakis, M.; Ye, L.; Tang, C. C.; Mpourmpakis, G.; Tsang, S. C. E., *Angew. Chem. Int. Ed.* **2016,** 55 (42), 13061-13066.
(37) Lo, B. T. W.; Ye, L.; Qu, J.; Sun, J.; Zheng, J.; Kong, D.; Murray, C. A.; Tang, C. C.; Tsang, S. C. E., *Angew. Chem. In. Ed.* **2016,** 55 (20), 5981-5984.
(38) Ye, L.; Teixeira, I.; Lo, B. T. W.; Zhao, P.; Tsang, S. C. E., *Chem. Commun.* **2017,** 53 (70), 9725-9728.
(39) Coelho, A. A. *TOPAS-Academic*, 4.1; Coelho Software, Brisbane.: 2007.
(40) Nguyen, C. M.; De Moor, B. A.; Reyniers, M.-F.; Marin, G. B., *J. Phys. Chem. C* **2011,** *115* (48), 23831-23847.
(41) Bond, G. C., *Heterogeneous Catalysis: Principles and Applications*. 2nd ed.; Oxford University Presss: 1987.

Table of Contents artwork